Semi-Analytical Model of Parasitic Capacitance of Inductor with Conductive Core

Florentin Salomez, Arnaud Videt, Nadir Idir

Semi-Analytical Model of Parasitic Capacitance of Inductor with Conductive Core

Florentin Salomez, Arnaud Videt, Nadir Idir

Univ. Lille, Arts et Metiers Institute of Technology, Centrale Lille, Junia, ULR 2697 - L2EP, F-59000 Lille, France

Corresponding author: Florentin Salomez, florentin.salomez@univ-lille.fr

Abstract

The stray capacitance of inductors impairs their high frequency impedance. A semi-analytical model is proposed for inductors with conductive core to gain insight for ways to decrease stray capacitance for high frequency power electronic applications. First the elementary capacitances are simulated thanks to 2D electrostatic finite element method (FEM), then an energetic approach is used to compute the global stray capacitance. Experimental verification has been performed on a nanocrystalline ring core. Relative error to the measurement shows that the proposed model improves the accuracy, notably by properly taking into account spaces between turns and between turns and core.

1 Introduction

Knowing the stray capacitance of inductors is important for high frequency power converters and especially in filtering applications [1]. Prediction of the stray capacitance is possible thanks to FEM [2]–[5], but analytical models are computationally faster, and more suited for optimization of the component volume [6]. The model presented by Massarini et al. in [7], and used in [8], [9], makes strong assumptions like tight windings and free voltage distribution that are generally not met for ring core inductors. This paper proposes to impose a linear distribution of the potential along the winding, as usually done in FEM, and as the models presented in [5], [10] would suggest. Then the stray capacitance is computed thanks to an energetic approach [11], [12] and [13, Sect. 11.6]. Firstly the geometry and the assumptions are detailed. Secondly the elementary capacitances are extracted thanks to FEM to take into account the spacing between turns, and between core and turns. Thirdly the model is derived and the model in [7] is adapted for comparison purpose. Finally the models are compared against experimental measurements performed on nanocrystalline cores and for several numbers of turns, a sensitivity analysis explains the origin of the deviation noticed between measurements and the proposed model.

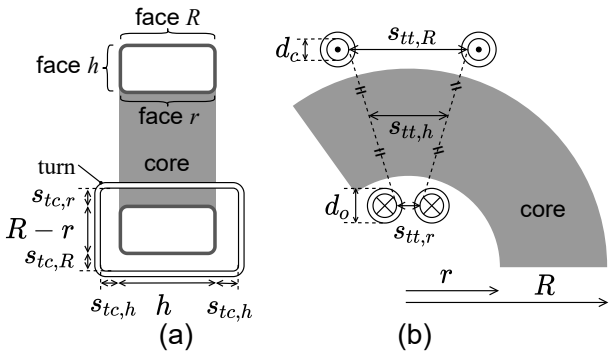

Fig. 1: Wound ring core geometry: (a) diameter cut, (b) close-up on a pair of turns

2 Geometry and electrical assumptions

The considered inductor is described hereafter. Only ring cores are studied in this paper.

2.1 Geometry and materials of the wound ring-core

An uncoated core of internal radius r, external radius R and height h is presented in fig. 1. An enamel copper wire of uncoated diameter d_c and of coated diameter d_o is wound N times around the core. The spaces between turn and core s_{tc}, and between turns s_{tt} are assumed constant along the faces. The suffix r, R, h are added regarding the

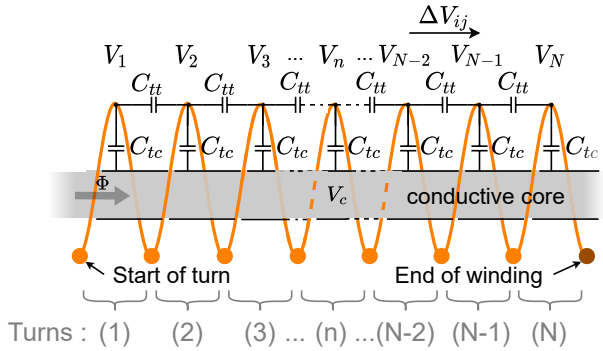

Fig. 2: Parasitic capacitances network

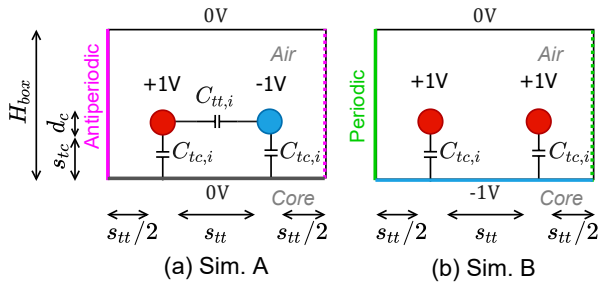

Fig. 3: Elementary parasitic capacitance simulation: (a) to extract C_{tt} knowing (b) C_{tc}

face considered. The core studied in this paper is considered as a perfect conductor (nanocrystalline material). The propagation of the electromagnetic wave along the winding is not modelled here. So the presented model of the inductor with one parallel stray capacitance holds until the quarter wave frequency of the total winding length. The relative permittivity of the wire enamel $\epsilon_r = 5$ [14] is neglected, but the spaces are still defined between conductors, this is the reason why in fig. 1 the thickness of the enamel is included into them.

2.2 Parasitic capacitances network

The previously presented wound component is unfolded around its revolution axis in fig. 2. Each turn n of the winding is approximated as a closed-loop of potential V_n and length p, and the core is at a floating potential V_c. Two conductors at different potentials who faces each other produce a capacitive coupling. Therefore this is modelled by two parasitic capacitances C_{tt} and C_{tc}, respectively for inter-turn and turn-core couplings.

3 Models of the elementary parasitic capacitances

The elementary parasitic capacitances are determined either by an analytical formulation or with FEM. The latter allows to take into account inter-turn and turn-core spaces.

3.1 Analytical models

In [7] the parasitic capacitance C_{tt} is modelled according to the approximated path of the electric field lines as presented in eq. (1). Only tight wound inductors are taken into account in [7] leading to the eq. (2). This approach works well in comparison to finite element method (FEM) only when d_c is small and s_{tt} is null [15].

$$\begin{cases} \theta' = \arccos\left(1 - \frac{\ln d_o/d_c}{\epsilon_r}\right) \\ C_{tt} = \epsilon_0 p \left(\frac{\epsilon_r \theta'}{\ln d_o/d_c} + \cot\frac{\theta'}{2} - \cot\frac{\pi}{12}\right) \end{cases} \quad (1)$$

$$C_{tc} = 2 \cdot C_{tt} \quad (2)$$

3.2 Finite-Element Method model

Since electrical coupling takes place in the air between the core and the turns, and between turns, 2D FEM on each face i of the core is used to extract C_{tt} and C_{tc} taking into account the space s_{tt} and s_{tc}. The geometries described in fig. 3 are implemented in FEMM 4.2. The space s_{tt} is small in regard of the core mean radius, therefore the core surface is considered locally flat. The equivalent capacitance of fig. 3 (a) is $C_{tt,i} + C_{tc,i}/2$ and the one of fig. 3 (b) is $2 \cdot C_{tc,i}$. Capacitances $C_{tc,i}$ and $C_{tt,i}$ are computed thanks to eq. (3) knowing the energy of each setup E_{SimA} and E_{SimB} respectively. These two simulations are repeated along each face (inner radius r, outer radius R and top and bottom h) with the corresponding s_{tt} and s_{tc} and the results are summed as in eq. (4)

$$\begin{cases} C_{tc,i} &= \frac{1}{4} E_{SimB} \\ C_{tt,i} &= \frac{1}{2} E_{SimA} - \frac{1}{8} E_{SimB} \end{cases} \quad (3)$$

$$\begin{cases} C_{tc} &= C_{tc,R} + C_{tc,r} + 2 \cdot C_{tc,h} \\ C_{tt} &= C_{tt,R} + C_{tt,r} + 2 \cdot C_{tt,h} \end{cases} \quad (4)$$

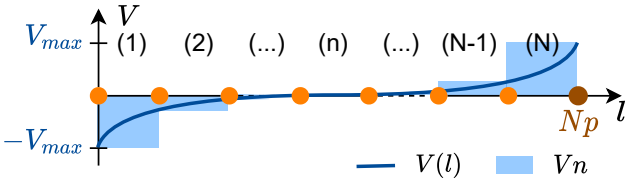

Fig. 4: Potential distribution along the winding for the Massarini et al. model

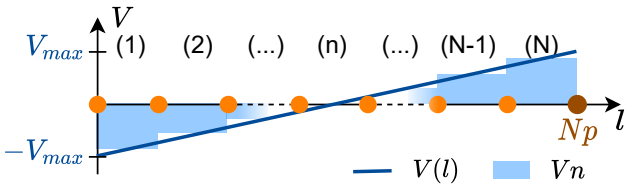

Fig. 5: Potential distribution along the winding with magnetic behaviour

4 Models of the stray capacitance

Once the parasitic capacitances are determined, the global stray capacitance can be derived. Two major assumptions are compared after to solve the parasitic capacitances network.

4.1 Massarini et al. model

According to Massarini et al. in [7] the electrical behaviour of the component is decoupled from the magnetic one. So the stray capacitance of the inductor is computed from the capacitance network in fig. 2 thanks to successive ΔY transformations that leads to the recursive sequence C_m described in [7, eq. (19)]. In this paper the sequence is generalized for $C_{tc} \neq C_{tt}$ to allow a fair comparison of the models. The new obtained sequence is called C_{gm} (*gm* stands for *Generalized Massarini*) and presented in eq. (5) with $N \in \mathbb{N}$. One can retrieve the original sequence C_m by injecting eq. (2) in eq. (5).

$$\begin{cases} C_{gm}(2) = C_{tt} + \frac{1}{2}C_{tc} \\ C_{gm}(3) = \frac{1}{2}C_{tt} + \frac{1}{2}C_{tc} \\ C_{gm}(N) = \frac{C_{tt}}{2+\frac{C_{tt}}{C_{gm}(N-2)}} + \frac{1}{2}C_{tc} \end{cases} \tag{5}$$

With this model the potentials V_2 to V_{N-1} are floating and the potential distribution will look like in fig. 4 with l the position on the total length of wire, and p the perimeter of one loop.

However each turn sees the same magnetic flux Φ as depicted in fig. 2, therefore the potential distribution will look more like in fig. 5, as explained in the following section.

4.2 Proposed model

To tackle the coupling problem between magnetic and electric behaviour, the proposed model imposes a linear potential distribution as shown in fig. 5 with each potential V_k defined as the mean potential of the n_{th} turn, see eq. (6), and with $\Delta V = 2V_{max}/N$ in case of symmetric voltage excitation. The core potential V_c is the mean excitation potential as in eq. (7) because of the symmetry of the network [16].

$$V_n = -V_{max} + \frac{\Delta V}{2} + (n-1)\Delta V \tag{6}$$

$$V_c = \frac{V_1 + V_N}{2} \tag{7}$$

Then an energetic approach as in [16] and in [13, Sect. 11.6] is applied to compute the total energy E_{tot} stored in the network eq. (8). Then eq. (8) is injected in eq. (9) (knowing that excitation voltage is equal to $2 \cdot V_{max}$) to obtain the stray capacitance C_{lin} as a function of the parasitic capacitances and the number of turns as in eq. (10).

$$E_{tot} = \sum_{n=1}^{N} \frac{1}{2}C_{tc}(V_n - V_c)^2 + \sum_{n=1}^{N-1} \frac{1}{2}C_{tt}\Delta V^2 \tag{8}$$

$$C_{lin} = \frac{E_{tot}}{2V_{max}^2} \tag{9}$$

$$C_{lin} = \frac{N-1}{N^2}C_{tt} + \frac{1}{12}\frac{N^2-1}{N}C_{tc} \tag{10}$$

5 Comparison of the models against measurements

The presented models of the stray capacitance are compared against measurements to assess the validity of the assumption regarding potential distribution along the winding. The stray capacitances are

Tab. 1: Measured variables

	min [mm]	mean [mm]	max [mm]
R	-	13.57	-
r	-	9.17	-
h	-	10.05	-
c	-	4.40	-
h_b	12.46	12.60	12.84
c_b	7.72	8.05	8.50
d_c	-	0.50	-
d_o	-	0.60	-
$s_{tc,PLA}$	-	0.50	-

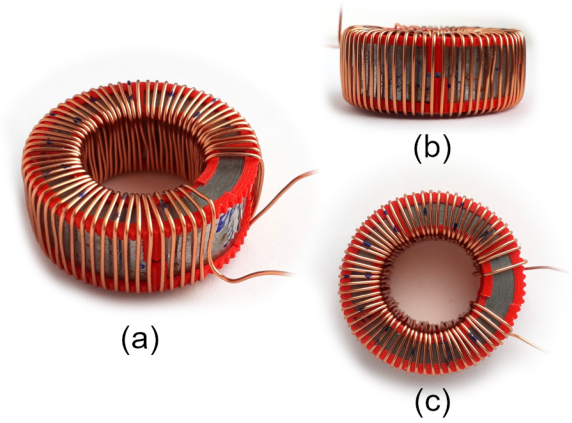

Fig. 6: Wound core : (a) perspective view, (b) side view, (c) top view

measured for several N and before unwinding geometrical measurements are performed to determine the parasitic capacitances C_{tt} and C_{tc}. A nanocrystalline core (*TCT TNA002BP19*) without its plastic case is used hereafter. It is equipped with turns spacer 3D printed with thermoplastic Polylactiv Acid (PLA) to maintain regular inter-turn and turn-core spacings and to protect wire insulation from the sharp edges of the core, as shown in fig. 6.

5.1 Geometrical measurements

The same core, wound and not wound, is measured with a caliper. Results are presented in table 1. Winding is not perfect so the mean values measurements are kept as nominal values, the table 1 shows also minimum and maximum values that will be used for a sensitivity analysis presented below. The distances s_{tt} and s_{tc} are not measurable directly, they are computed and presented in table 2. First the curvature of the turn, as depicted

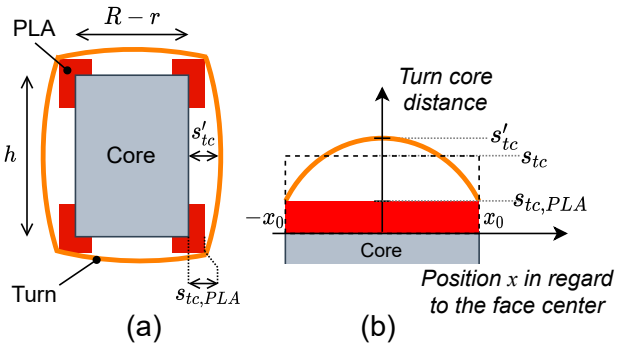

Fig. 7: Turn-core distance approximation : (a) radial cut of the inductor, (b) mean s_{tc}

in fig. 7 is not taken into account in the 2D FEM simulation. So the maximum turn-core spaces s'_{tc} are deduced from measurements thanks to eq. (11) then the approximated curvature in eq. (12) is used to compute the mean $s_{tc,i}$ in eq. (13). Second the inter-turn spaces $s_{tt,i}$ are deduced in eq. (14) from the winding angle β measured on the wound core (here 324 °).

$$\begin{cases} s'_{tc,r} &= \frac{1}{2}\left(c_b - c - d_o - d_c\right) \\ s'_{tc,h} &= \frac{1}{2}\left(h_b - h - d_o - d_c\right) \end{cases} \tag{11}$$

$$s_{tc}(x) = \left(s'_{tc} - s_{tc,PLA}\right)\left(1 - \frac{x}{x_0}^2\right) + s_{tc,PLA} \tag{12}$$

$$\begin{cases} s_{tc,r} &= s_{tc,R} = \frac{2}{3}s'_{tc,r} + \frac{1}{3}s_{tc,PLA} \\ s_{tc,h} &= \frac{2}{3}s'_{tc,h} + \frac{1}{3}s_{tc,PLA} \end{cases} \tag{13}$$

$$\begin{cases} s_{tt,r} &= \frac{1}{N-1}\left(\beta\left(r_b + \frac{d_o}{2}\right) - d_o\right) - d_c \\ s_{tt,R} &= \frac{1}{N-1}\left(\beta\left(r_b - \frac{d_o}{2}\right) - d_o\right) - d_c \\ s_{tt,h} &= \frac{1}{2}\left(s_{tt,r} + s_{tt,R}\right) \end{cases} \tag{14}$$

5.2 Stray capacitance measurement

The equivalent circuit of the wound component is shown in fig. 8 with R and L the resistive and inductive part respectively that are dependant of frequency and number of turns N, and C the stray capacitance in parallel. Its impedance is measured with an impedance analyzer (*HP 4294A* with *16047E* adapter) with a gap of 2.5 cm between the adapter and the component. To extract C from the

Tab. 2: Computed variables

	min [mm]	mean [mm]	max [mm]
R_b	15.23	15.40	15.62
r_b	7.51	7.34	7.12
$s'_{tc,r}$	1.11	1.28	1.50
$s'_{tc,h}$	0.66	0.73	0.85
$s_{tc,r}$	0.91	1.02	1.17
$s_{tc,h}$	0.60	0.65	0.73
$s_{tt,r}$	0.22	0.20	0.18
$s_{tt,R}$	0.93	0.95	0.97
$s_{tt,h}$	0.57	0.57	0.57

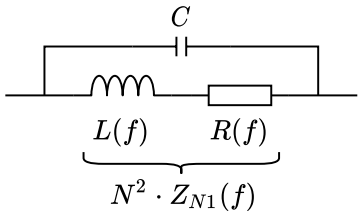

Fig. 8: Equivalent circuit of the inductor

impedance measurement the ideal impedance Z_{N1} without C must be known. It is retrieved from the impedance measurement at a low number of turns, $Z_{N1} = Z_{N5}/5^2$ assuming that the parasitic capacitance is negligible at such low turn number. Curve fitting is used to minimize the relative error between the model impedance $Z_{mod}(f, C)$ in eq. (15) (with $Z_C(f)$ the impedance of the stray capacitance C) and the measured one $Z_{meas}(f)$ with C as a decision variable. The frequency range for the fitting goes from 10 kHz to the quarter wave frequency of the wire length. The procedure is repeated every five turns while unwinding.

$$Z_{mod}(f, C) = \frac{N^2 Z_{N1}(f) \cdot Z_C(f)}{N^2 Z_{N1}(f) + Z_C(f)} \qquad (15)$$

5.3 Evolution of the stray capacitance regarding number of turns

To compare the different models presented in section 4 the geometry described in section 5.1 is modelled with 2D FEM as shown in section 3.2, with the mean values from table 1 and table 2. The permittivity of the PLA is neglected. Then the obtained elementary capacitances are injected into eq. (5) for C_{gm} and eq. (10) for C_{lin}. The model C_m

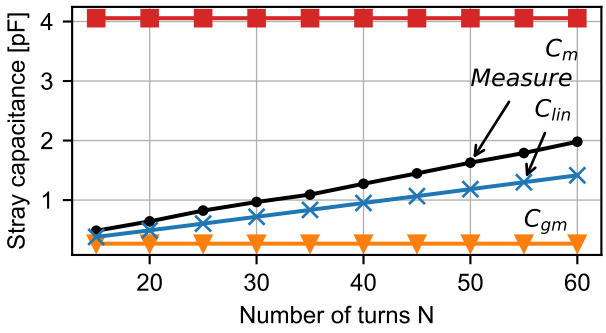

Fig. 9: Comparison of the models against measured stray capacitance for several numbers of turns N.

from [7] is computed thanks to eq. (1), (2) and (5). The results presented in fig. 9 show that this last model overestimates the stray capacitance by a factor of approximately 2 to 8. This result is expected because no turn-core and inter-turns spaces were taken into account. But the adapted one C_{gm} that takes into account these spaces, while not enforcing any potential distribution, does not reproduce the increase of the stray capacitance with the number of turns. Nevertheless the order of magnitude is better (factor of approximately 1/2 to 1). Finally the proposed model gives a correct order of magnitude (rel. error $< 30\%$) and reproduces the increase of stray capacitance with N. Thus the linear potential distribution hypothesis is rather verified. The deviation observed between measurements and the proposed model are investigated hereafter with the study of the effect of the plastic spacers on the stray capacitance and a sensitivity analysis regarding the inter-turn and turn-core spaces.

5.4 Effect of the plastic spacer on the measurements

The PLA spacers used to wind the component have a relative permittivity ϵ_{PLA} of 3 [17], and the part of the core perimeter covered by them is approximately 22%. 3D FEM is used to check how much the hypothesis leads to an underestimation of the C_{tc}. One outer quarter of a turn is modelled in *Comsol 5.4* electrostatic workbench with the geometry and boundary condition depicted in fig. 10. The core is considered locally straight, and the curvature of the turn is neglected apart around the spacer. Turn-core space $s_{tc,3D}$ is computed thanks to eq. (16),

Tab. 3: Capacitance from 3D FEM

ϵ_{PLA}	C [pF]	Relative Error
1	0.1	-20%
3	0.125	Ref.

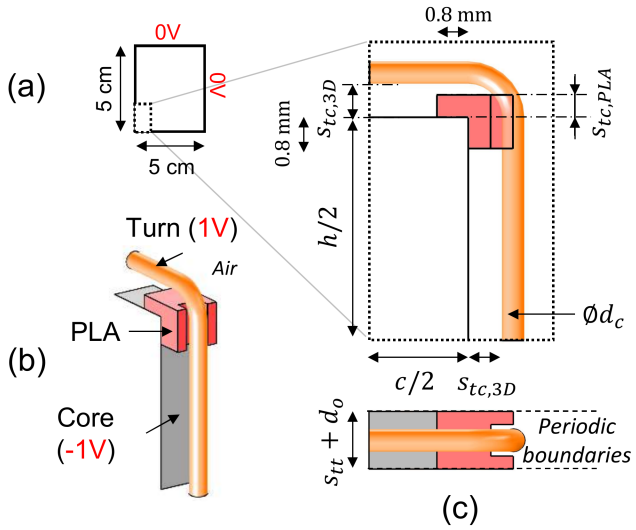

Fig. 10: Geometry of the outer quarter turn used in Comsol 5.4: (a) side view of the simulation domain, (b) 3D view, (c) close up of the side and top view.

and is equal to 0.76 mm. The simulation results in table 3 show that C_{tc} is underestimated by 20% when the ϵ_{PLA} is neglected. Thus the deviation noticed previously seems mainly due to the plastic spacer permittivity neglected in the model.

$$s_{tc,3D} = \sqrt{2} \cdot s_{tc,PLA} + \frac{d_o - d_c}{2} \tag{16}$$

Based on these FEM results a rough correction is applied to the turn-core capacitance value in the proposed model by multiplying the C_{tc} value by 1.25. This leads to the corrected stray capacitance $C_{lin,corr}$.

5.5 Sensitivity analysis

The accuracy of the inter-turn and turn-core spaces is also of great importance for the correct determination of parasitic capacitances C_{tc} and C_{tt}. This is why the minimum and maximum values presented in table 1 and table 2 are used to get a confidence interval around the nominal results presented before. The relative error to measurement are then

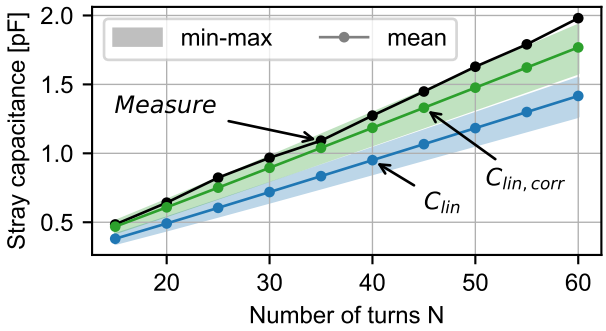

Fig. 11: Sensitivity analysis on the proposed model

22% and 36% for respectively the best and the worst case. Applying the estimated correction due to PLA presented previously, the relative error between the model and the measurements decreases to 5% and 20% for respectively the best and worst case. These results are illustrated in fig. 11. This sensitivity analysis shows that although the accuracy of s_{tt} and s_{tc} are important, the presence of a dielectric material between the turn and the core are of greater impact on the final value of the stray capacitance. Therefore the coating usually applied on the ring core is not negligible, and the wire coating might account for a small part of the measured capacitance value.

This results is also depicted in fig. 12 where the measured impedance is presented alongside the modelled ones for $N = 50$ turns. The grey curve is the impedance Z_L of the component without considering its stray capacitance C. It shows that the determination of the stray capacitance is of great importance for filter design. Since the relative error on the impedance of a capacitance due to the deviation Δ_C on the capacitance itself is $-\Delta_C/(1+\Delta_C)$, it is better to overestimate the stray capacitance value. Indeed C_m is an overestimation of nearly 150% but is closest to the measured impedance in comparison to the underestimation of approximately 80% produced by C_{gm}. Finally, as stated in section 2.1 the second resonance at about 55 MHz present in the measurement (black curve) is not reproduced by the models because the propagation of the electromagnetic wave along the wire is not modelled here. Still, the proposed semi-analytical model based on elementary capacitances is valid in this example up to 30MHz.

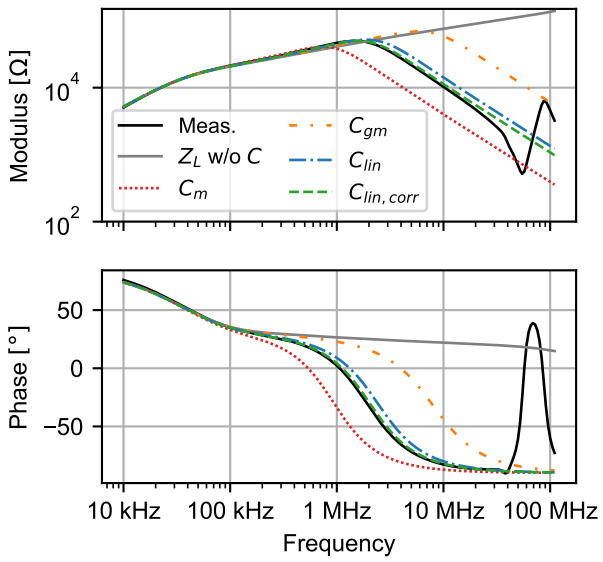

Fig. 12: Comparison between measurement and models of the impedance for $N = 50$.

6 Conclusion

The proposed model gives a good estimation of the stray capacitance of the nano crystalline inductor based on the FEM determination of the parasitic inter-turn and turn-core capacitances. The increase of the stray capacitance with the increase of the number of turns for one given core is correctly predicted by this model. In addition it takes into account the inter-turn and turn-core spaces. The perspectives of this work are first the study of the impact of coatings on the total value of the stray capacitance, then the analysis of the available degree of freedom for its minimization, and finally the generalization of the model to other material like ferrites. This model applied to filtering inductors like common-mode chokes would improve their optimal sizing for high frequency applications.

Acknowledgment

This work has been achieved within the framework of CE2I project (Convertisseur d'Energie Intégré Intelligent). CE2I is co-financed by European Union with the financial support of European Regional Development Fund (ERDF), French state and the French Region of Hauts-de-France.

References

[1] A. K. Morya, M. C. Gardner, B. Anvari, L. Liu, A. G. Yepes, *et al.*, "Wide bandgap devices in ac electric drives: Opportunities and challenges," *IEEE Transactions on Transportation Electrification*, vol. 5, no. 1, pp. 3–20, 2019. DOI: 10.1109/TTE.2019.2892807.

[2] Qin Yu and T. W. Holmes, "A study on stray capacitance modeling of inductors by using the finite element method," *IEEE Transactions on Electromagnetic Compatibility*, vol. 43, no. 1, pp. 88–93, 2001. DOI: 10.1109/15.917948.

[3] M. Kovacic, S. Stipetic, Z. Hanic, and D. Zarko, "Small-signal calculation of common-mode choke characteristics using finite-element method," *IEEE Transactions on Electromagnetic Compatibility*, vol. 57, no. 1, pp. 93–101, 2015. DOI: 10.1109/TEMC.2014.2362998.

[4] C. Cuellar and N. Idir, "Stray capacitances determination methods of emi filter inductors," in *IECON 2017 - 43rd Annual Conference of the IEEE Industrial Electronics Society*, 2017, pp. 7040–7045. DOI: 10.1109/IECON.2017.8217231.

[5] A. Chafi, N. Idir, A. Videt, and H. Maher, "Design method of pcb inductors for high-frequency gan converters," *IEEE Transactions on Power Electronics*, vol. 36, no. 1, pp. 805–814, 2021. DOI: 10.1109/TPEL.2020.3000438.

[6] B. Zaidi, A. Videt, and N. Idir, "Optimization method of cm inductor volume taking into account the magnetic core saturation issues," *IEEE Transactions on Power Electronics*, vol. 34, no. 5, pp. 4279–4291, 2019. DOI: 10.1109/TPEL.2018.2861620.

[7] A. Massarini and M. K. Kazimierczuk, "Self-capacitance of inductors," *IEEE Transactions on Power Electronics*, vol. 12, no. 4, pp. 671–676, 1997. DOI: 10.1109/63.602562.

[8] B. Touré, J. Schanen, L. Gerbaud, T. Meynard, J. Roudet, and R. Ruelland, "Emc modeling of drives for aircraft applications: Modeling process, emi filter optimization, and technological choice," *IEEE Transactions on Power Electronics*, vol. 28, no. 3, pp. 1145–1156, 2013. DOI: 10.1109/TPEL.2012.2207128.

[9] A. Roc'h, H. Bergsma, D. Zhao, B. Ferreira, and F. Leferink, "A new behavioural model for performance evaluation of common mode chokes," in *2007 18th International Zurich Symposium on Electromagnetic Compatibility*, 2007, pp. 501–504. DOI: 10.1109/EMCZUR.2007.4388305.

[10] M. Kovacic, Z. Hanic, S. Stipetic, S. Krishnamurthy, and D. Zarko, "Analytical wideband model of a common-mode choke," *IEEE Transactions on Power Electronics*, vol. 27, no. 7, pp. 3173–3185, 2012. DOI: 10.1109/TPEL.2011.2182060.

[11] W. Tan, X. Margueron, and N. Idir, "Analytical modeling of parasitic capacitances for a planar common mode inductor in emi filters," in *2012 15th International Power Electronics and Motion Control Conference (EPE/PEMC)*, 2012, DS3f.2-1-DS3f.2–6. DOI: 10.1109/EPEPEMC.2012.6397368.

[12] J. Biela and J. W. Kolar, "Using transformer parasitics for resonant convertersa review of the calculation of the stray capacitance of transformers," *IEEE Transactions on Industry Applications*, vol. 44, no. 1, pp. 223–233, 2008. DOI: 10.1109/TIA.2007.912722.

[13] E. C. Snelling, *Soft Ferrites : Properties and Applications*. London: Iliffe Books Ltd, 1969.

[14] M. Jomaa, L. Seveyrat, L. Lebrun, K. Masenelli-Varlot, and J. Cavaille, "Dielectric properties of segmented polyurethanes for electromechanical applications," *Polymer*, vol. 63, pp. 214–221, 2015, cited By 10. DOI: 10.1016/j.polymer.2015.03.008.

[15] N. B. Chagas and T. B. Marchesan, "Analytical calculation of static capacitance for high-frequency inductors and transformers," *IEEE Transactions on Power Electronics*, vol. 34, no. 2, pp. 1672–1682, 2019. DOI: 10.1109/TPEL.2018.2829716.

[16] Z. Shen, H. Wang, Y. Shen, Z. Qin, and F. Blaabjerg, "An improved stray capacitance model for inductors," *IEEE Transactions on Power Electronics*, vol. 34, no. 11, pp. 11 153–11 170, 2019. DOI: 10.1109/TPEL.2019.2897787.

[17] J. Zechmeister and J. Lacik, "Complex relative permittivity measurement of selected 3d-printed materials up to 10 ghz," in *2019 Conference on Microwave Techniques (COMITE)*, 2019, pp. 1–4. DOI: 10.1109/COMITE.2019.8733590.